Medical Science Journal for Advance Research

Copyright © The Author(s)
Vol. 7, No. 2, June 2026
e-ISSN: 2774-4892

Eco-friendly Synthesis of Silver Nanoparticles Using *Lantana camara* Extract and Their Antimicrobial Potential Against *Escherichia coli*

Sarmed M. Hussein
Tropical-Biological Research Unit, College of Science, University of Baghdad, Baghdad, Iraq.
***e-mail:** Sarmed.m@sc.uobaghdad.edu.iq

ABSTRACT

Background: *Agar well inhibition zones combine biological response with material transport and release.* ***Aim:*** *We examine recorded characterization images and a four-level zone matrix for ten selected Escherichia coli isolates exposed to a Lantana camara silver preparation.* ***Methods:*** *The optical spectrum has a maximum near 445 nm, EDX identifies silver in the analyzed region, and five FE-SEM annotations span 55.67–91.46 nm.* ***Results:*** *All ten isolates show increasing visible diameters across the three higher nominal concentrations, with means of 12.79, 18.75 and 24.21 mm; five have no visible zone at the lowest concentration. Six of 45 comparable isolate pairs reverse order between the fully visible endpoints. A shared-slope log-label description has an internal omitted-dose RMSE of 1.05 mm, but does not reproduce these reversals. A finite-source mathematical model explains why endpoint zones alone cannot separately identify transport, release, growth-critical time, releasable mass and inhibitory threshold. Across 120 generated groups per mechanism, median synthetic extrapolation error increases from 0.37 to 0.76 mm under misspecified mass availability.* ***Conclusion:*** *An independent published matrix provides a separate example of dose-dependent isolate ordering. The case supports a descriptive concentration trend and limits on its interpretation. Regional characterization and nominal concentration labels do not establish delivered active-silver mass, nanoparticle-specific activity or clinical efficacy.*

Keywords: Agar Well Diffusion; Inhibition Zone; Silver Nanoparticles; *Escherichia Coli*; Censored Observations; Simulation.

Article Information
Received: April 28, 2026; Revised: May 25, 2026; Online: June 2026y

INTRODUCTION

The diameter of a growth-free region depends on how much active material reaches the agar, how far it moves before the organism forms a visible lawn and what concentration arrests growth. Diffusion theory and earlier agar-bioassay models formalize this relationship [1–3]. A recent experimental analysis of biosynthesized silver particles also links disc-zone kinetics to silver-ion release [4]. A visually convincing concentration trend can consequently coexist with uncertainty about actual silver mass, ionic release, source geometry and organism-specific threshold. These are different unknowns that a single endpoint photograph cannot independently reveal.

Experimental comparisons also caution against assigning a nanoparticle mechanism from a diffusion zone alone. Kourmouli et al. linked the apparent response in their silver-particle disc tests to released ions and the distinct mobility of dissolved species [5]. Cavassin et al. evaluated diffusion screening alongside separately determined antimicrobial endpoints, illustrating that the chosen readout is part of the interpretation [6]. These findings motivate a bounded reading of an inhibition-zone matrix: a detectable preparation-level effect does not by itself identify the active silver species or define a quantitative endpoint for another assay.

https://doi.org/10.46966/msjar.v7i2.430
This work is licensed under a Creative Commons Attribution 4.0 International License

Prior studies describe *Lantana camara* mediated silver preparations tested against *E. coli* [7–11]. The present study combines the recorded optical, elemental and surface characterization with a ten-isolate inhibition-zone matrix. Its computational component examines which physical quantities can be identified from those endpoint observations, building on established structural and practical identifiability analysis [12]. A separate published agar-well matrix for a different plant-mediated material [13] provides a second test of dose ordering and model behavior; measurements from the two preparations are analyzed separately.

Characterization introduces a related distinction. Studies of silver colloids document particulate, dissolved and surface-associated silver, while single-particle observations show that aggregation and dissolution can evolve together [14,15]. Complementary spectroscopic studies resolve chemical transformations and surface composition that cannot be assigned from particle appearance or an elemental abundance alone [16,17]. These observations provide context for interpreting the present image exports individually, without transferring a chemical-state assignment or a dissolution rate from another material.

We examine the recorded concentration trend and whether isolate ordering persists across dose labels. Internal dose-omission checks assess three compact descriptions of the same matrix. A finite-source model and explicitly generated scenarios then test the interpretation of endpoint zones and extrapolation. A separate published matrix provides an independent example of the analysis. These components distinguish the observed case from mathematical results and do not pool measurements from different preparations.

METHODS

Experimental records and computational analyses

Table 1. Three noninterchangeable sources used in this manuscript.

Source	Material and observations	Use in this analysis
Supplied case study	Ten selected *E. coli* isolates; four nominal levels; UV, EDX, FE-SEM and AFM image exports	Descriptive case data and within-table checks
Published Barabadi et al. [13]	Eleven pathogenic *E. coli* strains as described by the authors and ATCC 25922; 12 × 4 published zone table	Independent analysis-pipeline stress test; no pooled coefficients
Generated mathematical scenarios	120 ten-isolate groups per assumed mechanism with known inputs; additional simulated high dose	Sensitivity and model-error counterexamples; no new experiments

Preparation and experimental measurements

The original study describes 10 g of air-dried *L. camara* leaf powder extracted in 100 mL water at 70 °C for 30 min. A 10 mL aliquot of filtered extract was mixed with 90 mL of 1 mM $AgNO_3$ at 50 °C and pH 9 for 24 h. The reported stock was prepared from dried material and used for serial dilution. The labels 15.6, 31.2, 62.5 and 125 µg/mL are retained as nominal preparation concentrations; they are not converted into elemental-silver or nanoparticle doses. The stated reagent inputs correspond to 0.09 mmol $AgNO_3$ entering the reaction, which is distinct from the delivered mass after drying and dilution.

The study record describes 55 *E. coli* urine isolates from several hospitals, of which ten were selected following a crystal-violet microplate screen. The analysis uses one displayed diameter per selected isolate at each of four nominal labels. Additional source labels of 3.9 and 7.8 µg/mL are outside this tabulated matrix. Each cell is treated as a reported summary observation; variation among dose levels or selected isolates is not interpreted as technical-repeat precision. The source describes an agar well assay with a 24 h endpoint and reports no zone for the distilled-water control. The plate photograph provides qualitative context. Analysis is restricted to the tabulated zones and does not classify the selected isolates as MDR or establish biofilm-specific or bactericidal effects. The distinction between variation among conditions and independent replication follows the experimental-unit reasoning discussed by Hurlbert [18].

Analysis of the supplied zone matrix

A table entry of zero at 15.6 µg/mL was encoded as no visible zone (ND), with no numeric diameter or assumed visibility limit. Zone means, within-isolate differences and the bootstrap of isolate

 Copyright © The Author(s)

resampling use the higher three levels where all ten have reported zones. The bootstrap resamples ten isolate rows 6,000 times with a fixed seed and describes only the composition of this selected group; it does not estimate technical precision or population uncertainty. Resampling follows the empirical-distribution rationale of the bootstrap [19]. Because the isolates were selected, this calculation does not account for their selection mechanism; broader inference would require additional assumptions about selection [20].

Three descriptive candidates use ten isolate intercepts and one shared slope each. Their response forms are shown below, where C is the nominal concentration label and Z is the reported diameter. The squared-radius candidate is an idealized shape, not a physical transport coefficient. All fits use the three fully visible levels. Each complete dose group is omitted in turn and predicted after refitting the other two groups; errors are scored on diameter. The initial radius fit minimizes squared-radius residuals. A sensitivity analysis minimizes diameter residuals with nonnegative radius intercepts and slope; the separate published-data fit constrains its intercept using the reported well radius. Endpoint omissions are extrapolations and the middle omission is interpolation. A held-isolate check uses that isolate's measured lowest fully visible level as a calibration baseline. The unused lowest nominal level is scored only for its five visible observations. These internal checks are not independent experimental replications. Dependence between observations and the prediction target affect the interpretation of cross-validation [21]. Here, a missing dose response for an already observed isolate and a baseline-calibrated response for a held-out isolate are explicitly different targets.

$$Z_{ij} = \alpha_i + \beta \log_2(C_j / 31.2)$$
$$Z_{ij} = \gamma_i + \delta(C_j / 31.2 - 1)$$
$$(Z_{ij} / 2)^2 = a_i + b \ln(C_j / 31.2)$$

We also count endpoint rank reversals among isolate pairs with unequal reported zones at both fully visible endpoints. A shared slope with isolate-specific intercepts forces the same isolate order at every dose for an additive diameter model and for its strictly increasing squared-radius transform. For the independent published matrix, subtracting each row and column mean and adding the grand mean yields the exact residual of the least-squares additive diameter model $Z_{ij}=\alpha_i+g_j$, which allows an unrestricted shared effect at each measured dose. Its in-sample RMSE is a lower bound for any additive diameter model with an isolate intercept and a common dose curve, not for nonlinear radius models fitted in diameter space. A separate 12-slope published-data fit permits one linear concentration slope per strain and uses the same four whole-dose omission folds as the shared-slope linear fit. With only three other dose groups per fold, this is a diagnostic of extrapolation, not a selected final model. Hypothetical per-cell perturbations of ±0.5 and ±1 mm quantify reversals guaranteed under those bounds; neither interval estimates measurement error.

Finite source model and structural identifiability

For the mathematical analysis, consider a homogeneous thin layer, a uniform circular source of radius a and one soluble inhibitory species. Let D denote effective transport, t* the time at which the boundary is fixed, k a first-order release rate and M_j the initially releasable mass at level j. The plate-reading time is distinct from t* [1]. The surface density is (M_j/a^2) F (ρ; τ, κ), where F integrates the two-dimensional Gaussian kernel over the disc and the assumed release history. With ρ = r/a, $\tau = Dt^*/a^2$, κ = kt* and $\theta = \sigma^* a^2/Mref$, the boundary satisfies the equation below. Here σ* is an areal inhibitory threshold and Mref is a reference releasable mass. This equation supplies a theoretical counterexample to identifiability; it is not calibrated to the selected isolates.

$$(M_j / Mref)\, F(\rho; \tau, \kappa) = \theta$$

For positive s such that both proposed critical times remain within the assay interval, replacing (D, t*, k) with (sD,t*/s,sk) leaves τ and κ unchanged. For any positive q, multiplying every initially releasable M_j, Mref and σ* by q leaves every mass ratio and θ unchanged. Therefore, both transformations preserve every predicted boundary and diameter exactly for fixed a. Even perfect zone measurements at arbitrarily many labels cannot resolve these rescaled quantities under this model; independently measured inputs are required. If a and layer thickness are also unknown, further ambiguity arises. The numerical kernel uses Gauss–Legendre integration and verifies its immediate-release centre limit and selected doubled-quadrature calculations. A 13 × 13 dimensionless (τ,κ) grid illustrates the relation at illustrative θ=0.025 and relative masses 1 and 4; no field is fitted to EC1–EC10.

For a separate, single-isolate hypothetical design, let the physical parameter vector be (ln D, ln t*, ln k, ln Mref, ln σ*), with source radius and dose mass ratios provisionally fixed. Zone sensitivities factor as J=GB, where G is sensitivity to (ln τ, ln κ, ln θ) and the three rows of B are (1,1,0,0,0), (0,1,1,0,0), and (0,0,0,−1,1). Thus J has two exact null directions before numerical evaluation. A finite-difference Jacobian and assumed independent measurements of t* and of the initially releasable effective Mref test which added observables can break these symmetries; total silver alone would leave its

Copyright © The Author(s)

unknown releasable fraction unresolved. Rank is an exact local question, whereas illustrative error-normalized singular values and inverse-information standard deviations examine practical precision. This design does not estimate the ten isolates' parameters [12].

Generated stress test under dose and visibility misspecification

The reproducible generator assumes a 3 mm source radius, τ=2.10, κ=1.70 and independent normally distributed 0.27 mm perturbations to latent apparent diameters. It creates 120 independent synthetic ten-isolate groups per mechanism with shared random seeds. Relative nominal labels are 0.5, 1, 2, 4 and 8; the ratio 8 (250 µg/mL if mapped to this case) is exclusively an invented stress-test level. Each group calibrates a separate threshold-to-mass ratio for each synthetic isolate using its observed ratio-1 baseline, then selects a shared (τ,κ) from a stated 19 × 18 grid using ratio-2 and ratio-4 values. The ratio-0.5 and ratio-8 outcomes are withheld. The first generator makes available mass proportional to the label q; the second uses $q/[1+0.12(q-1)]$ but is fitted with the proportional model. Fixed thresholds of 8, 9.5 and 11 mm are tried as hypothetical visibility rules; none is the measured threshold for the supplied plates. This is a sensitivity experiment under declared assumptions, not a training set of additional clinical isolates.

Independent published table as an analysis stress test

Barabadi and colleagues published a four-dose agar-well table for a *Pimpinella anisum* seed-mediated silver preparation in eleven *E. coli* strains described as pathogenic and one reference strain [13]. Their methods report an 8 mm well and a 100 µL aliquot at each of 128, 256, 512 and 1024 µg/mL. We transcribed all 48 published cell values, counted strict and nondecreasing within-strain trajectories, and counted pairwise rank reversals between endpoint doses only among pairs without an endpoint tie. We additionally count reversals whose endpoint order is guaranteed under hypothetical bounded changes of each reported cell by ±0.5 or ±1.0 mm; these bounds are sensitivity scenarios, not estimated measurement errors. The publication gives one number per strain and dose despite a general statement about repeats; raw within-condition readings and their variation are unavailable. The nominal doses, matrix chemistry, isolates and geometry differ from the supplied case, so we do not pool zone sizes, fit a common physical coefficient or call it biological validation of *L. camara*.

The accompanying code reproduces the case-table fits, finite-source calculations, generated scenarios and separate published-table checks. The workflow uses NumPy, SciPy and Matplotlib, with data origins and random seeds stated in the scripts. Statistical summaries remain descriptive for the selected case group; source images are retained unchanged.

RESULTS

Optical elemental and surface characterization

The recorded optical trace has a broad maximum near 445 nm (Figure 1). This observation describes the supplied spectrum and is not used to quantify elemental-silver concentration, purity or particle-size distribution.

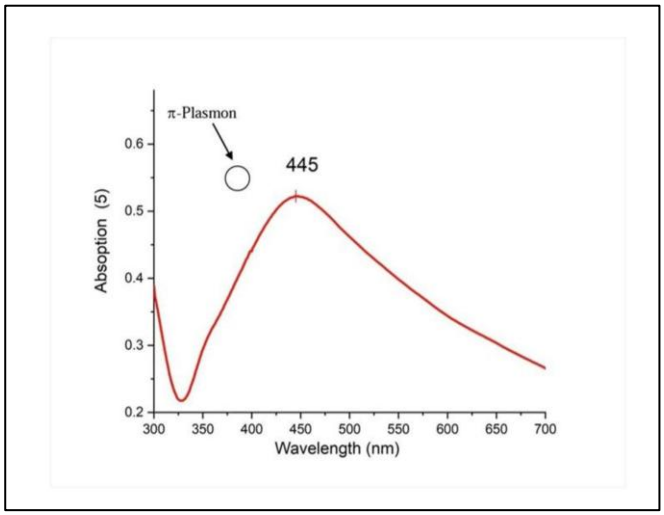


Figure 1. Recorded optical spectrum with a broad maximum near 445 nm. *The source image is reproduced without modification.*

The EDX spectrum contains a silver signal near 3 keV (Figure 2). The analyzed field contains 2.9 atomic% and 17.9 weight% Ag (Table 2). These values describe the measured region; they are not the silver mass fraction delivered to the assay. The software error columns are retained with their original labels and are not treated as replicate standard deviations.

Copyright © The Author(s)

Table 2. EDX composition of the analyzed field. Error columns reproduce the software output and are not interpreted as repeat-measurement standard deviations.

Element	Atomic %	Reported error	Weight %	Reported error
C	48.2	0.7	33.1	0.5
N	10.2	1.8	8.1	1.4
O	32.5	1.0	29.7	0.9
Na	1.3	0.1	1.7	0.2
Mg	1.3	0.1	1.8	0.1
Al	0.9	0.0	1.4	0.1
Ca	2.8	0.1	6.3	0.1
Ag	2.9	0.1	17.9	0.3

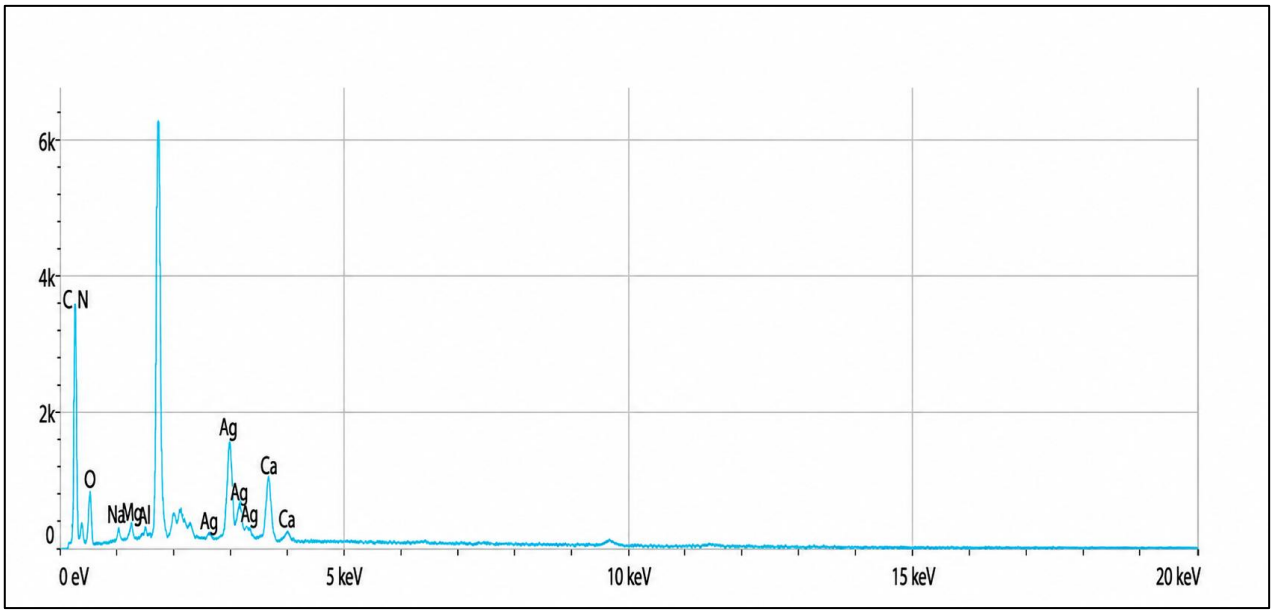


Figure 2. Recorded EDX spectrum of the analyzed region.

The FE-SEM export shows five annotated lateral feature dimensions between 55.67 and 91.46 nm (Figure 3). These annotations describe the marked features in the displayed field and are not a particle-size distribution.

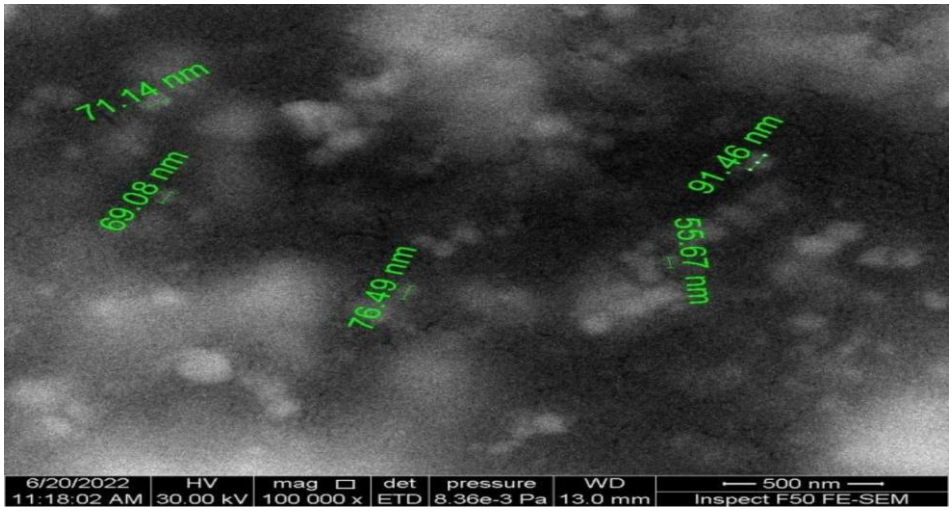


Figure 3. FE-SEM field with five annotated lateral feature dimensions between 55.67 and 91.46 nm. These selected features do not constitute a particle-size distribution.

Copyright © The Author(s)

The AFM export presents surface topography over 0.50 × 0.50 µm (Figure 4). Its height legend extends from 0 to 14.1 nm. This scale describes the displayed height range and is not a particle diameter or an average roughness value.

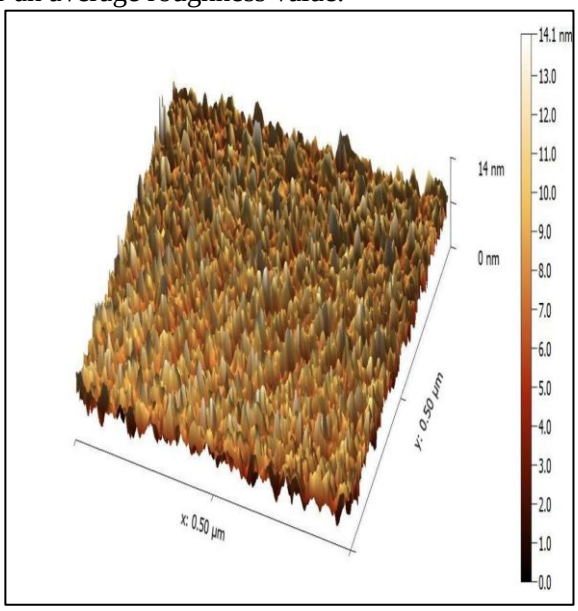


Figure 4. Recorded AFM topography over 0.50 × 0.50 µm with a displayed height scale from 0 to 14.1 nm.

Table 3 retains every supplied isolate-level zone. All ten showed larger visible diameters at each of the three higher nominal levels; five had no visible zone at 15.6 µg/mL. Means across ten reported diameters were 12.79, 18.75 and 24.21 mm at 31.2, 62.5 and 125 µg/mL. No mean is computed for the lowest label because ND is not a measured zero diameter. The mean paired increases were 5.96 and 5.46 mm for consecutive higher steps. These are descriptions of selected isolates, not estimates of repeat-to-repeat laboratory precision.

Table 3. Recorded apparent inhibition-zone diameters in millimetres. *ND denotes no visible exterior zone rather than a measured zero diameter.*

Isolate	15.6 µg/mL	31.2 µg/mL	62.5 µg/mL	125 µg/mL
EC1	ND	11.5	18.5	22.3
EC2	ND	13.5	17.8	24.2
EC3	11.5	14.8	21.6	28.33
EC4	10.2	12.2	19.4	26.5
EC5	ND	10.8	16.5	21.8
EC6	12.4	13.9	20.2	25.1
EC7	13.8	15.6	22.1	27.4
EC8	ND	11.2	15.8	20.9
EC9	11.1	12.5	18.2	23.6
EC10	ND	11.9	17.4	22
Mean	—	12.79	18.75	24.21

The recorded plate photograph is shown in Figure 5. Its wells have no isolate or nominal-level labels, so the image is used as a qualitative experimental record; the numerical analysis uses the tabulated diameters.

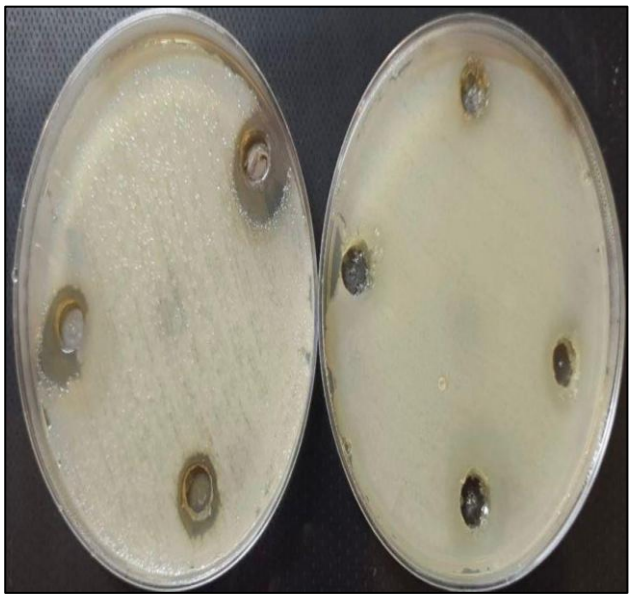


Figure 5. Recorded agar plate photographs with unlabeled wells.

Descriptive model checks and isolate ranking

Between 31.2 and 125 µg/mL, 6 of 45 isolate pairs change order despite every isolate increasing its own zone; 2 of those reversals persist for all hypothetical independent per-cell changes bounded by ±0.5 mm, and none is guaranteed at ±1.0 mm. These uncertainty envelopes are algebraic, not measured repeat precision. The three shared-slope candidates predict no isolate-rank reversal at all across doses, so even the locally best held-out RMSE does not make them adequate for dose-independent susceptibility ranking.

All descriptive summaries and model checks are recalculated from the displayed isolate-level cells. Source summary columns are audited separately in Supplementary Table 2. The analysis makes no significance claim based on across-dose or across-isolate dispersion.

Copyright © The Author(s)

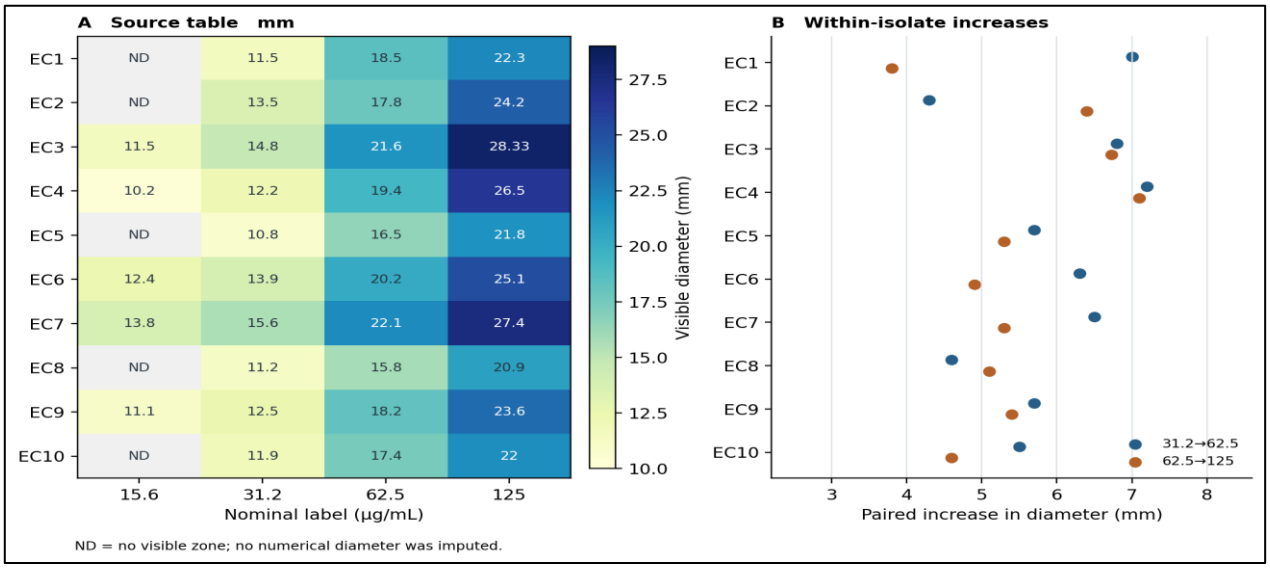


Figure 6. Supplied ten-isolate matrix and paired changes. *ND is a qualitative nondetection at the lowest nominal label. The right-hand differences use two fully detectable steps.*

Table 4. Within-isolate changes computed from the supplied matrix. The resampling interval reflects variation in selected isolate rows, not uncertainty in laboratory repeat readings.

Nominal step µg/mL	Mean Δ diameter mm	Isolate resampling 95% mm	Mean Δ annulus mm²
31.2 to 62.5	5.96	5.36–6.54	148.9
62.5 to 125	5.46	4.87–6.07	185.9

Among the three equal-complexity functional forms in Table 5, diameter versus $\log_2$ nominal label had the smallest dose-omission RMSE of 1.05 mm, compared with 4.44 mm for a linear label and 3.06 mm for the original transformed-response squared-radius fit. Re-optimizing the radius form directly against diameter residuals reduced its error to 2.55 mm, leaving the model ranking unchanged. The log-label model's shared fitted gain was 5.71 mm per approximate twofold step; its 95% isolate-resampling interval was 5.31–6.15 mm. Withholding a dose leaves only two dose groups to fit a slope, so even the smallest RMSE is a fragile, internal predictive score.

Table 5. Three equal-complexity descriptive forms, each with one shared slope and ten isolate intercepts; the radius form is shown under two fitting losses.

All errors are scored on diameter, but original radius parameters were fitted on squared radius. The refit minimizes diameter residuals. The diameter-loss refit has no calibrated-isolate score.

Candidate	Fit RMSE mm	Omitted dose RMSE mm	Calibrated isolate RMSE mm
Diameter vs $\log_2$ label	0.65	1.05	1.30
Diameter vs linear label	1.18	4.44	2.09
Radius²: fit on radius²	1.25	3.06	1.74
Radius²: fit on diameter	1.03	2.55	—*

Copyright © The Author(s)

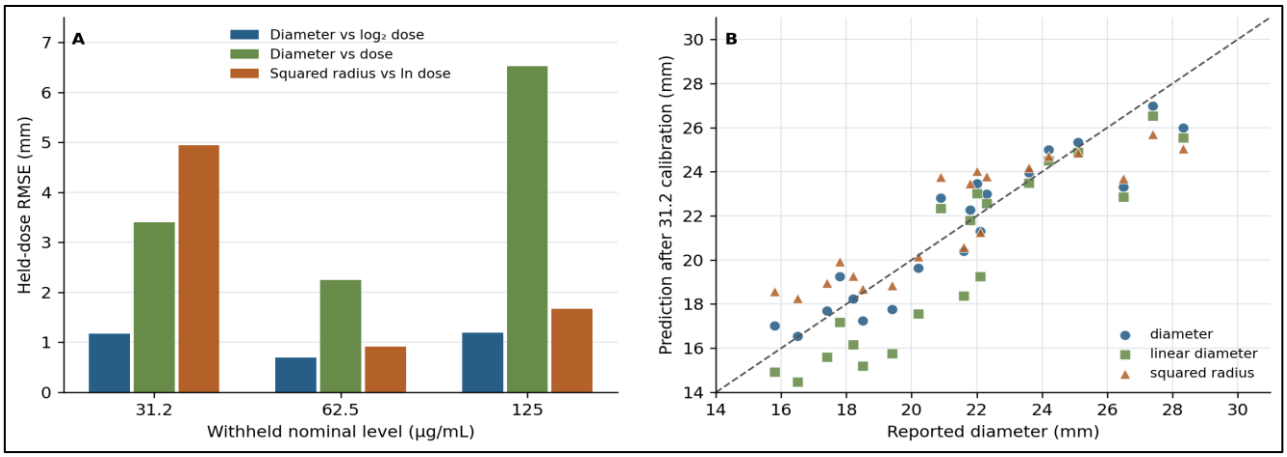


Figure 7. Internal candidate checks on the supplied matrix. *The omitted-dose panel includes endpoint extrapolations; the held-isolate panel uses its measured 31.2 µg/mL value to calibrate each tested isolate.*

The best high-dose descriptive curve was then evaluated at the unused 15.6 µg/mL label. Among only the five isolates with a visible observation, conditional RMSE was 3.33 mm and mean predicted-minus-observed diameter was -3.12 mm. Five remaining observations were ND, with no diameter residual. Figure 8 displays no fictitious zero-valued points at that label; selection on visibility precludes using the conditional error as an error estimate for all ten isolates.

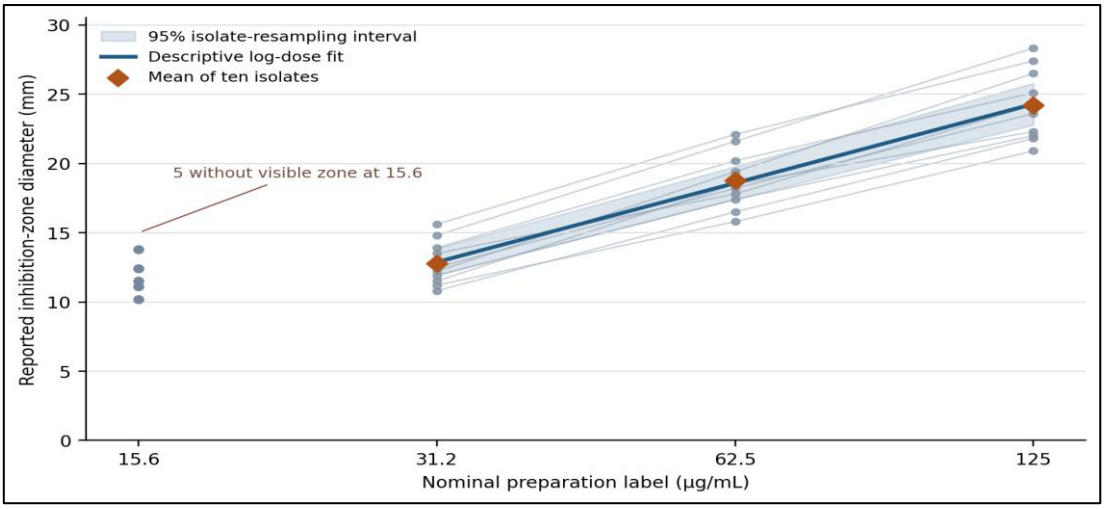


Figure 8. Measured high-dose diameters and a within-range descriptive log-label curve, with isolate-resampling band. *Five low-dose zones were visible; the other five are annotated as nondetections and are not plotted as zeros. The curve was fitted only to the higher three labels.*

Exact physical ambiguity and synthetic counterexamples

Table 6 summarizes two exact symmetries of the stated finite-source model. Since predicted values coincide for every radius and mass ratio, a smaller residual or more dose points cannot distinguish members of either equivalence class. The existing supplied data cannot identify physical D, release k, growth-critical time t*, initially releasable mass or inhibitory threshold; this follows from the equations even before assay noise is considered.

Table 6. Structural nonidentifiability for a fixed source radius and thin-layer model.

q is positive; s also keeps both candidate t values inside the assay interval. Changes refer to hypothetical inputs, not the observed data.*

Simultaneous transformation	Unchanged combinations	Consequence for all predicted zones
$D \rightarrow sD$; $t^* \rightarrow t^*/s$; $k \rightarrow sk$	Dt^*/a^2 and kt^*	Identical transport and release shape at the effective growth-critical time.
Releasable $M_j \rightarrow qM_j$; $M_{ref} \rightarrow qM_{ref}$; $\sigma^* \rightarrow q\sigma^*$	M_j/M_{ref} and $\sigma^* a^2/M_{ref}$	Identical boundary despite changed initial releasable mass and threshold

Copyright © The Author(s)

In an intentionally uncalibrated dimensionless grid, changing τ and κ gave an exterior-halo/source-radius range of 0.00–1.15 at assumed relative mass 1 and 0.45–2.77 at assumed mass 4 (Figure 9). The model can produce no exterior halo at the lower mass for settings that produce a halo at the higher one. Neither axes nor color scale represent silver diffusion measured in the supplied plates.

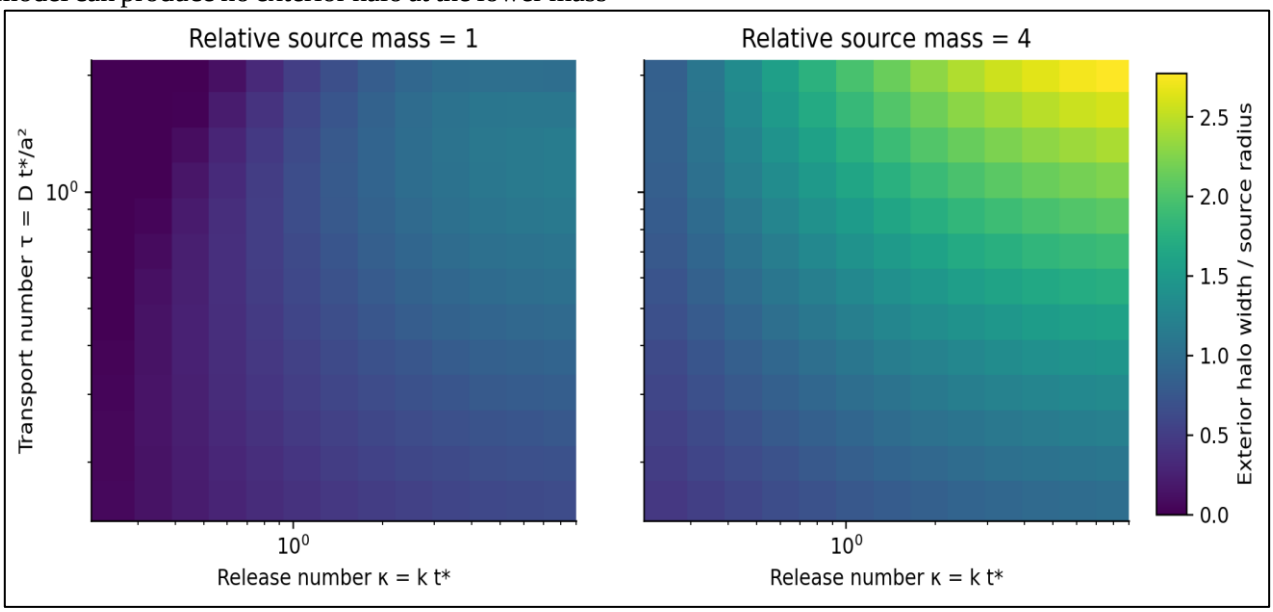


Figure 9. Numerical finite-disc, first-order release model for illustrative dimensionless τ, κ and θ=0.025. *Color is exterior halo width divided by source radius. No physical parameter was estimated from the reported bacteria.*

An additional synthetic experiment generated 120 independent ten-isolate groups for each assumed mass-availability law. Under the correctly specified proportional law, median fitted-group RMSE was 0.32 mm and median error at the synthetic withheld ratio-8 level was 0.37 mm. When the generator instead saturated while the fitted model still assumed proportional availability, corresponding medians were 0.34 and 0.76 mm. In 93.3% of matched generated groups the misspecified setting had greater high-dose error. These values are consequences of the explicitly chosen generator, noise law, grid and extrapolation distance, not accuracy estimates for the supplied experiment.

Table 7. Synthetic stress-test summary across 120 generated ten-isolate groups per mass law. *Training uses ratio 1 as measured baseline and ratios 2 and 4 as fit targets. Ratio 8 is held out and exists only in simulation.*

Generator mass availability	***Median training RMSE mm***	***Median withheld ratio 8 RMSE mm***
Proportional q	*0.32*	*0.37*
Saturating q/[1+0.12(q−1)]	*0.34*	*0.76*

For one generated group, 50 grid parameter pairs lay within an arbitrarily chosen 0.25 mm training-RMSE tolerance of the best pair. Their dimensionless release numbers spanned 0.45–5.20, and their mean predicted diameter at the invented 250 µg/mL label ranged from 24.76 to 26.61 mm. This is a discrete one-example sensitivity set under a selected tolerance, not a confidence interval or evidence for the true release coefficient.

Copyright © The Author(s)

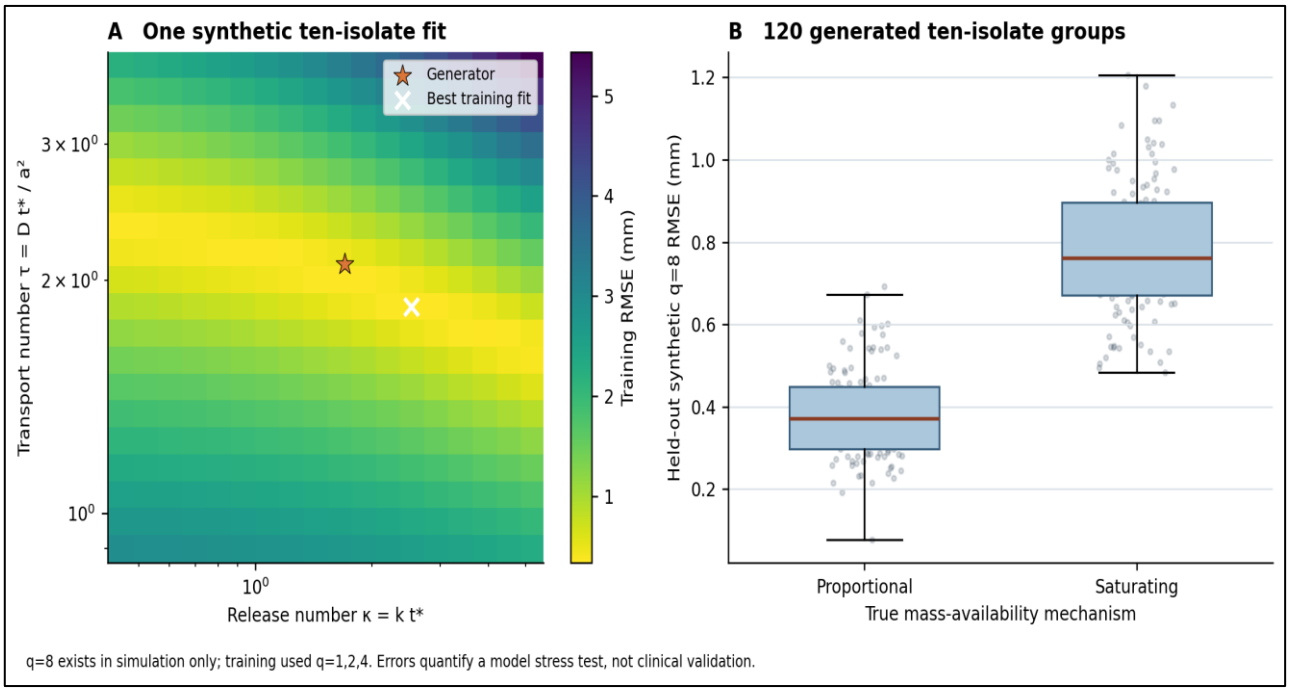


Figure 10. **Entirely generated model audit.** *The profile surface shows one simulated group and a tradeoff between τ and κ; the boxplots show held-out error in 120 generated groups for each specified mass law. Ratio 8 and every plotted synthetic isolate were invented for this stress test.*

A synthetic visibility boundary also changes the interpretation of an ND label. Under the proportional generator, visible low-dose zones occur in 66.0%, 22.9% and 3.9% of cases at hypothetical reporting boundaries of 8, 9.5 and 11 mm, respectively. These values belong to the generated scenario. The five observed nondetections in the case matrix remain qualitative ND entries and are not assigned zero diameters.

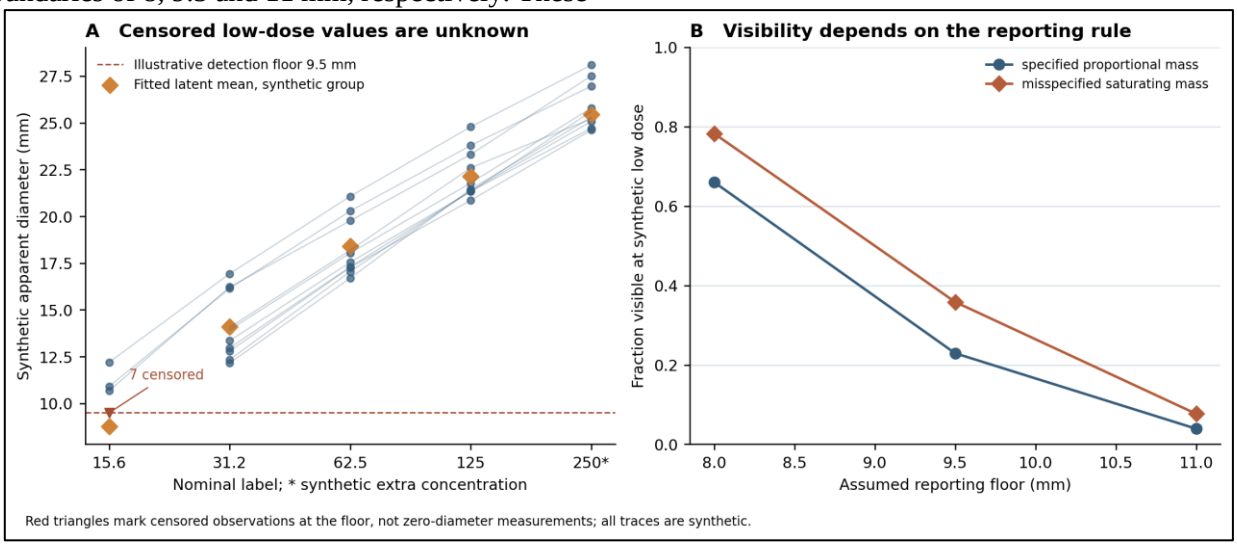


Figure 11. Entirely generated detection-rule experiment. *Red triangles show censored synthetic low-dose observations at an illustrative reporting boundary; they are not zero diameters. The additional 250 µg/mL label exists only within the mathematical scenario.*

In an additional one-isolate hypothetical design, the physical sensitivity matrix has rank 3/5 at three dose ratios and remains rank 3/5 at five. Adding a separate measurement of t* or effective initially releasable Mref raises the rank to four, while measuring both raises it to five (Figure 12). This is a locally sufficient measurement design under the specified five-parameter model, conditional on its fixed source geometry and five-parameter specification. With deliberately assumed independent zone SD 0.27 mm, log-time SD 0.05 and log-releasable-mass SD 0.10, the illustrative local linearized SD for ln k is still 0.50. These hypothetical error scales are not measured precision or confidence intervals for the supplied *E. coli* isolates.

 Copyright © The Author(s)

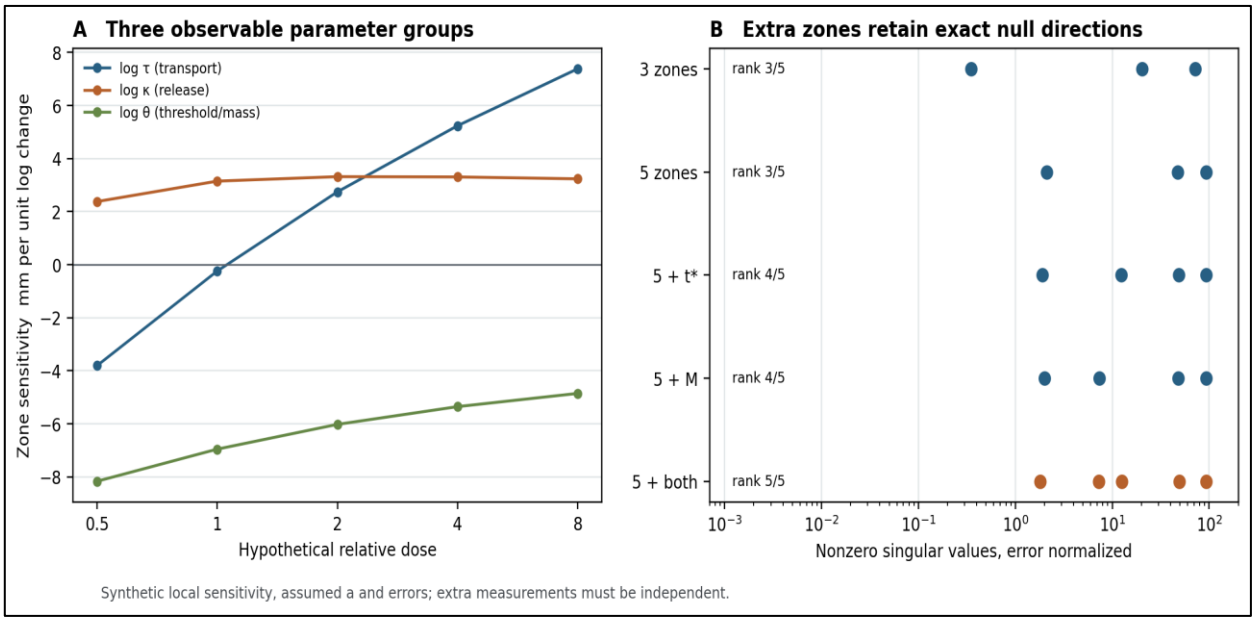


Figure 12. Hypothetical single-isolate design: five physical parameters, two exact null directions under zone data alone. *Independent measurements of growth-critical time and effective releasable mass each remove one direction. Singular values depend on assumed precision.*

Separate published data demonstrate dose dependent ranking

Every published strain in Table 8 [13] has a nondecreasing zone sequence (three plateaus, nine strictly increasing). Of 66 possible isolate pairs, 10 have an endpoint tie and 25 of the other 56 reverse rank between the lowest and highest doses: E1 changes 22→30 mm, E6 17→40 mm. These are independent published observations, not measurements of the supplied *L. camara* material.

Table 8. Reproduced numeric values from Barabadi et al. [13], Table 1, in millimetres (© 2023 the authors, CC BY 3.0). This is an attributed independent Pimpinella anisum silver preparation; its nominal mass labels must not be pooled with the supplied Lantana case.

Published strain	128 µg/mL	256 µg/mL	512 µg/mL	1024 µg/mL
E1	22	22	28	30
E2	20	22	25	37
E3	19	26	26	28
E4	18	19	20	23
E5	20	23	25	30
E6	17	19	28	40
E7	14	18	25	27
E8	18	20	21	30
E9	15	15	17	35
E10	15	17	19	32
E11	14	17	18	20
ATCC 25922	15	20	30	40

The median published diameter at the four concentrations was 17.5, 19.5, 25 and 30 mm. A wholly monotonic response within each strain therefore does not guarantee a dose-independent order across strains. The supplied case independently has six observed pairwise reversals, but the two preparations and isolate collections cannot be pooled or assumed biologically equivalent. Neither set of nominal labels establishes delivered active silver mass. Of the 25 strict observed reversals, 22 retain their opposite endpoint signs under any hypothetical per-cell change of at most ±0.5 mm and 17 under ±1.0 mm; these are algebraic bounds, not measured assay precision. Excluding ATCC 25922 leaves 19/48 reversed comparable pairs, so the result is not driven solely by the reference strain.

A parallel leave-one-whole-dose-out test on this separate published matrix changes the descriptive model ranking: linear-label diameter has 4.00 mm RMSE, compared with 5.09 mm for $\log_2$-label diameter and 7.86 mm for the originally transformed-loss squared-radius fit. That radius fit produces 6 nonphysical negative squared-radius held-out predictions that were bounded to zero for scoring. Refitting the same functional form on diameter loss and enforcing the reported 8 mm well reduces its score to 5.51 mm and avoids below-well predictions; the linear diameter form remains first. All three forms again have one shared slope and a separate intercept per strain. These are internal checks, not evidence that a response law transfers between studies.

Copyright © The Author(s)

Table 9. Whole-dose-omission comparison in the independent Barabadi et al. matrix [13]. *Three functional forms each have 12 strain intercepts and one common slope; the radius form is audited under both fitting losses. All 48 held-out cells are scored in diameter millimetres.*

Published-data candidate	Held-out RMSE mm	Held-out MAE mm	Nonphysical squared-radius cases
Diameter vs $\log_2$ label	5.09	3.99	0
Diameter vs linear label	4.00	3.23	0
Radius²: fit on radius²	7.86	6.02	6
Radius²: fit on diameter	5.51	4.29	0

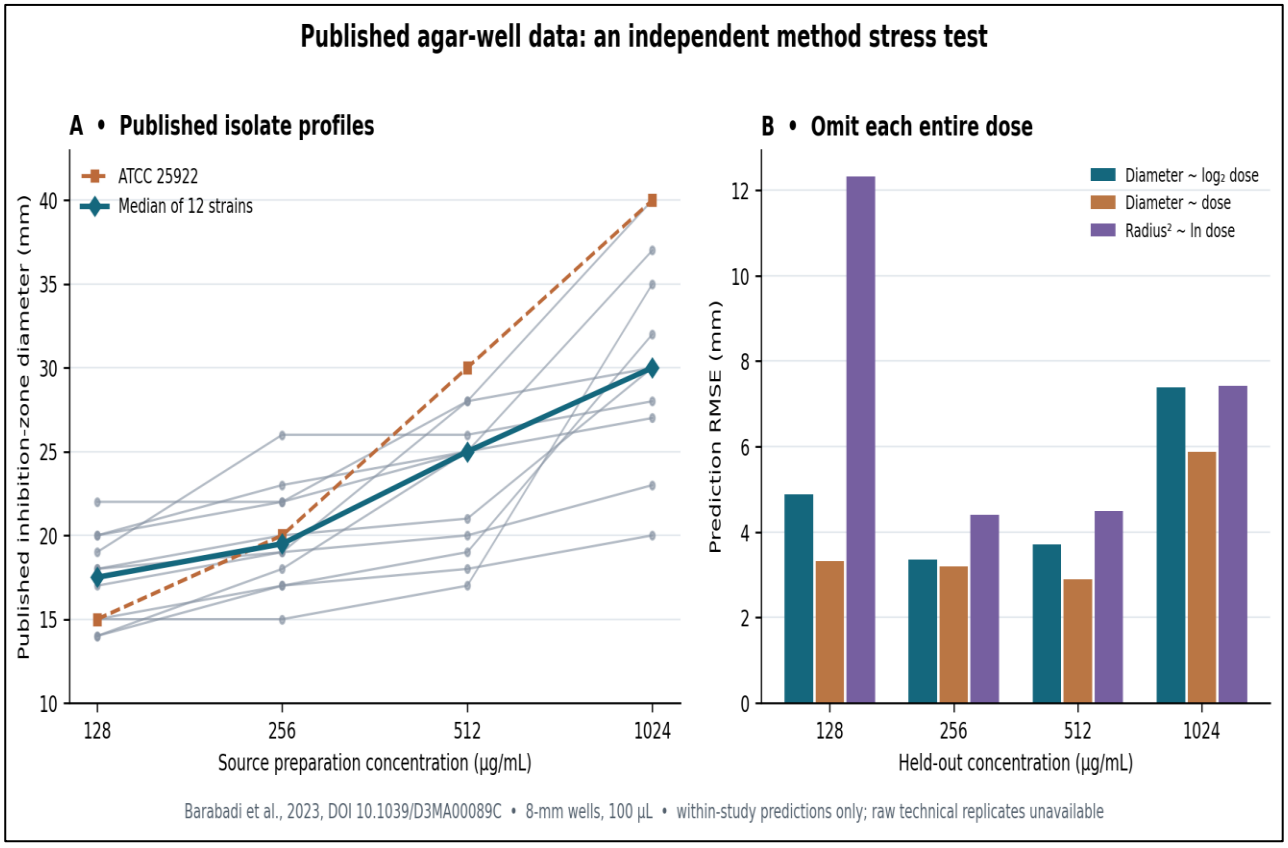


Figure 13. Barabadi et al. [13] Table 1 reanalysis (CC BY 3.0). Panel B plots the transformed-loss radius fit; its diameter-loss refit appears in Table 9.

Double centering all 48 published entries leaves an interaction sum of squares of 423.19 mm², or 20.1% of total cell variation, and a minimum in-sample RMSE of 2.97 mm for any diameter-additive isolate-intercept model with a shared, otherwise unrestricted dose effect (Figure 14). That lower bound does not apply to a nonlinear radius model measured in diameter. Giving each strain a separate linear concentration slope instead raised the identically folded whole-dose omission RMSE from 4.00 to 4.49 mm.

Thus the published matrix shows real variation that shared-slope additive curves cannot capture exactly, while four doses do not support a claim that 12 individually fitted slopes improve new-dose predictions; no inferential P value is attached to these descriptive source cells.

 Copyright © The Author(s)

Medical Science Journal for Advance Research

Copyright © The Author(s)
Vol. 7, No. 2, June 2026
e-ISSN: 2774-4892

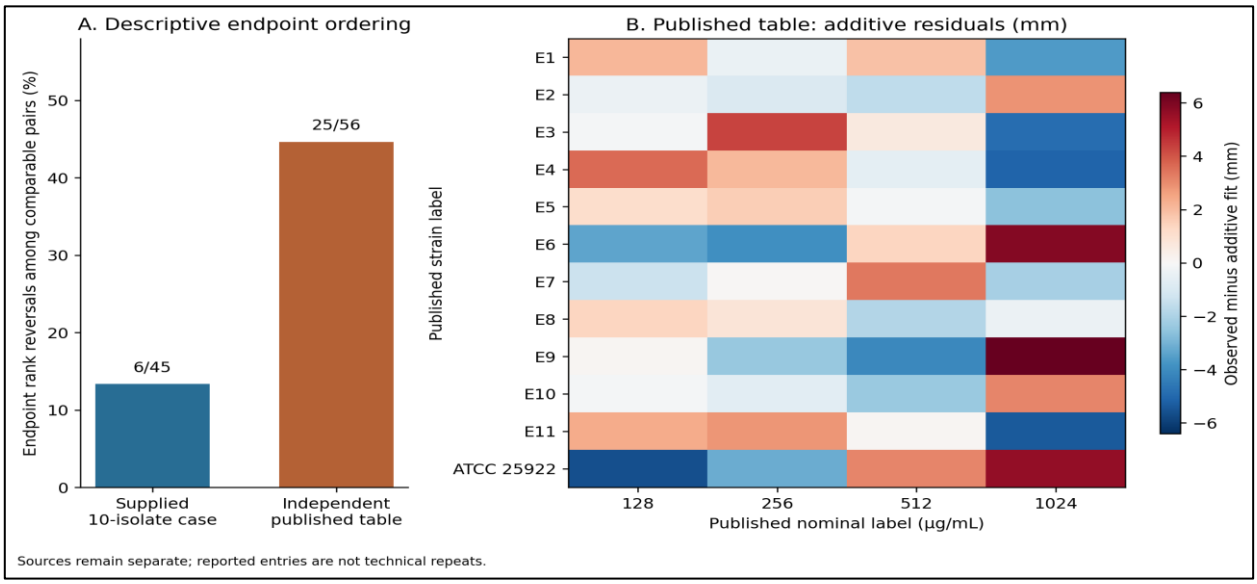


Figure 14. Separate arithmetic audits: observed endpoint isolate-order reversals in the supplied and published sources; *heatmap of residuals after the best unrestricted additive diameter fit to the independent Barabadi et al. [13] table (CC BY 3.0). Bars are different datasets and do not compare efficacy.*

A second independent well-assay report provides a different reporting example: Elshazly et al. [22] used a stated 10 mm well for a *Nigella sativa* silver preparation; its published *E. coli* dose series reports a 10 mm diameter at the lowest concentration. The reported number coincides with the well diameter and therefore does not, by itself, demonstrate any exterior inhibition halo. This is a separate published material and a qualitative geometry check, not an extra observation of the supplied Lantana batch or an estimate of its ND threshold.

DISCUSSION

The principal empirical finding is a concentration-associated increase in apparent zone diameter among the ten selected isolates, accompanied by changes in their pairwise ordering. This combination matters because a consistent within-isolate increase does not guarantee a stable comparison between isolates. The characterization exports provide optical, elemental and surface observations at their recorded scales; they do not quantify the active material reaching the inhibition boundary. Earlier work on agar transport, growth boundaries and silver-ion kinetics provides the mechanistic context [1–4], while assay comparisons demonstrate that test format affects interpretation [23].

The material observations constrain different questions. The EDX signal supports the presence of silver in the analyzed region, and the microscopy exports describe local morphology and topography.

Research resolving silver-particle surface transformations uses complementary chemical-state evidence [16,17]; those studies do not imply that the present preparation underwent the same transformation. Likewise, the partition of silver among particulate and other forms can change over time [14,15]. Consequently, the optical maximum and regional images cannot be used to assign the mass of the active species at the inhibition boundary. Published mechanism studies also support a context-dependent interpretation. Xiu et al. found negligible additional particle-specific activity in their tested systems after accounting for released ionic silver [24]. Sotiriou and Pratsinis attributed different relative contributions to ions and particles across their material variants [25]. Neither result establishes the mechanism in the present plant-derived preparation. Together with diffusion-test and assay-comparison studies [5,6], this literature supports describing the observed zones as responses to the tested preparation while keeping mechanistic attribution separate.

The log-label curve gives the smallest internal omission error among the three stipulated functional forms, including a radius-model sensitivity analysis using the same diameter loss. Its common slope still cannot reproduce observed order reversals. Low-dose scoring is conditional on visibility, and prediction for a held-out isolate requires its measured baseline. The independent published

https://doi.org/10.46966/msjar.v7i2.430
This work is licensed under a Creative Commons Attribution 4.0 International License
Published by: READ INSTITUTE

matrix illustrates the same ranking issue but favors a different descriptive curve; its measurements are neither pooled with the case nor treated as biological replication. Allowing a separate linear slope for each published strain worsens whole-dose omission error, showing that additional flexibility does not necessarily improve extrapolation. These scores address the particular omission schemes used here. Correlated-data cross-validation theory explains why an error estimate tied to one prediction setting should not automatically be interpreted as an error estimate for another [21].

The mathematical analysis explains a complementary limit. Two continuous parameter rescalings preserve every boundary of the stated finite-source mod el. Consequently, even exact endpoint zones identify composite quantities rather than the individual physical parameters. The generated scenarios give a further counterexample: a close training fit can coexist with larger extrapolation error when available mass departs from the assumed proportional relationship. Neither the simulated mass law nor its noise and visibility rules is an empirical finding about this preparation. The separate well-sized diameter example [22] reinforces the need to interpret a zone relative to its measurement geometry. Earlier model studies show that predictions of some observables may be well constrained while individual parameters remain uncertain [26]. That practical sensitivity issue is distinct from the exact structural symmetries demonstrated here; the interpretation of structural versus practical identifiability follows Raue et al. [12].

CONCLUSION

The recorded optical, elemental and surface features describe the silver-containing preparation, and the ten-isolate matrix shows increasing apparent zone diameters across three fully visible nominal levels. Pairwise order reversals and internal omission checks show that this trend does not establish a dose-independent isolate ranking or a transferable response law. Under the finite-source model, joint rescalings of diffusion, critical growth time and release, and of initially releasable mass and inhibitory threshold, preserve every predicted zone. The generated analyses make these ambiguities and extrapolation limits explicit. The experimental record and computation therefore support complementary descriptive and mathematical conclusions, without identifying nanoparticle-specific action.

REFERENCES

[1] Chandrasekar V, Knabel SJ, Anantheswaran RC. Modeling development of inhibition zones in an agar diffusion bioassay. Food Sci Nutr. 2015;3:394–403. doi:10.1002/fsn3.232.

[2] Cornette de Saint Cyr L, Ramadier G, Ruiz Valencia A, Méricq J-P, Soussan L. Mechanistic study of the kinetic phenomena influencing the bacteriostatic action of silver ions in agar bioassays. Antibiotics. 2021;10:368. doi:10.3390/antibiotics10040368.

[3] Bonev B, Hooper J, Parisot J. Principles of assessing bacterial susceptibility to antibiotics using the agar diffusion method. J Antimicrob Chemother. 2008;61:1295–1301. doi:10.1093/jac/dkn090.

[4] Carrapiço A, Pico M, Carreiro EP, et al. Biosynthesis of silver-based nanoparticles: Critical assessment of antimicrobial assays and diffusion kinetics analysis. Int Biodeterior Biodegrad. 2025;205:106167. doi:10.1016/j.ibiod.2025.106167.

[5] Kourmouli A, Valenti M, van Rijn E, Beaumont HJE, Kalantzi OI, Schmidt-Ott A, Biskos G. Can disc diffusion susceptibility tests assess the antimicrobial activity of engineered nanoparticles? J Nanopart Res. 2018;20:62. doi:10.1007/s11051-018-4152-3.

[6] Cavassin ED, de Figueiredo LFP, Otoch JP, et al. Comparison of methods to detect the in vitro activity of silver nanoparticles (AgNP) against multidrug resistant bacteria. J Nanobiotechnology. 2015;13:64. doi:10.1186/s12951-015-0120-6.

[7] Singh PK, Bhardwaj K, Dubey P, Prabhune A. UV-assisted size sampling and antibacterial screening of *Lantana camara* leaf extract synthesized silver nanoparticles. RSC Adv. 2015;5:24513–24520. doi:10.1039/C4RA17233G.

 Copyright © The Author(s)

[8] Ajitha B, Ashok Kumar Reddy Y, Sreedhara Reddy P. Green synthesis and characterization of silver nanoparticles using *Lantana camara* leaf extract. Mater Sci Eng C. 2015;49:373–381. doi:10.1016/j.msec.2015.01.035.

[9] Ajitha B, Ashok Kumar Reddy Y, Shameer S, Rajesh KM, Suneetha Y, Sreedhara Reddy P. *Lantana camara* leaf extract mediated silver nanoparticles: Antibacterial, green catalyst. J Photochem Photobiol B. 2015;149:84–92. doi:10.1016/j.jphotobiol.2015.05.020.

[10] Patil SP, Kumbhar ST. Antioxidant, antibacterial and cytotoxic potential of silver nanoparticles synthesized using terpenes rich extract of *Lantana camara* L. leaves. Biochem Biophys Rep. 2017;10:76–81. doi:10.1016/j.bbrep.2017.03.002.

[11] Aritonang HF, Koleangan H, Wuntu AD. Synthesis of silver nanoparticles using aqueous extract of medicinal plants' (*Impatiens balsamina* and *Lantana camara*) fresh leaves and analysis of antimicrobial activity. Int J Microbiol. 2019;2019:8642303. doi:10.1155/2019/8642303.

[12] Raue A, Kreutz C, Maiwald T, et al. Structural and practical identifiability analysis of partially observed dynamical models by exploiting the profile likelihood. Bioinformatics. 2009;25:1923–1929. doi:10.1093/bioinformatics/btp358.

[13] Barabadi H, Hosseini O, Jounaki K, et al. Bioinspired green-synthesized silver nanoparticles: in vitro physicochemical, antibacterial, biofilm inhibitory, genotoxicity, antidiabetic, antioxidant, and anticoagulant performance. Mater Adv. 2023;4:3037–3054. doi:10.1039/D3MA00089C. CC BY 3.0.

[14] Liu J, Hurt RH. Ion release kinetics and particle persistence in aqueous nano-silver colloids. Environ Sci Technol. 2010;44:2169–2175. doi:10.1021/es9035557.

[15] Jiang D, Chen HB, Zhou XL, Liu XW. Single-particle electrochemical imaging provides insights into silver nanoparticle dissolution at the solution–solid interface. ACS Appl Mater Interfaces. 2022;14:22658–22665. doi:10.1021/acsami.2c05148.

[16] Pettibone JM, Gorham JM, Liu J. Determining surface chemical composition of silver nanoparticles during sulfidation by monitoring the ligand shell. J Nanopart Res. 2018;20:312. doi:10.1007/s11051-018-4410-4.

[17] Levard C, Reinsch BC, Michel FM, Oumahi C, Lowry GV, Brown GE Jr. Sulfidation processes of PVP-coated silver nanoparticles in aqueous solution: impact on dissolution rate. Environ Sci Technol. 2011;45:5260–5266. doi:10.1021/es2007758.

[18] Hurlbert SH. Pseudoreplication and the design of ecological field experiments. Ecol Monogr. 1984;54:187–211. doi:10.2307/1942661.

[19] Efron B. Bootstrap methods: another look at the jackknife. Ann Stat. 1979;7:1–26. doi:10.1214/aos/1176344552.

[20] Copas JB, Li HG. Inference for non-random samples. J R Stat Soc Series B. 1997;59:55–95. doi:10.1111/1467-9868.00055.

[21] Rabinowicz A, Rosset S. Cross-validation for correlated data. J Am Stat Assoc. 2022;117:718–731. doi:10.1080/01621459.2020.1801451.

Copyright © The Author(s)

[22] Elshazly EH, Mohamed AKSH, Aboelmagd HA, et al. Phytotoxicity and antimicrobial activity of green synthesized silver nanoparticles using *Nigella sativa* seeds on wheat seedlings. J Chem. 2022;2022:9609559. doi:10.1155/2022/9609559.

[23] Chung E, Ren G, Johnston I, Matharu RK, Ciric L, Walecka A, Cheong YK. Applied methods to assess the antimicrobial activity of metallic-based nanoparticles. Bioengineering. 2023;10:1259. doi:10.3390/bioengineering10111259.

[24] Xiu ZM, Zhang QB, Puppala HL, Colvin VL, Alvarez PJJ. Negligible particle-specific antibacterial activity of silver nanoparticles. Nano Lett. 2012;12:4271–4275. doi:10.1021/nl301934w.

[25] Sotiriou GA, Pratsinis SE. Antibacterial activity of nanosilver ions and particles. Environ Sci Technol. 2010;44:5649–5654. doi:10.1021/es101072s.

[26] Gutenkunst RN, Waterfall JJ, Casey FP, Brown KS, Myers CR, Sethna JP. Universally sloppy parameter sensitivities in systems biology models. PLoS Comput Biol. 2007;3:e189. doi:10.1371/journal.pcbi.0030189.

 Copyright © The Author(s)